Influence of water radiolysis on the passive properties of 316Lstainless steel

Nicolas Bérerd, Nathalie Moncoffre, Philippe Martinet, Sabrina Marcelin, Dominique Baux, Bernard Normand

Influence of water radiolysis on the passive properties of 316L-stainless steel

Nicolas Bérerd[*,1,2], Nathalie Moncoffre[1], Philippe Martinet[1,3], Sabrina Marcelin[3], Dominique Baux[4] and Bernard Normand[3]

[1] Institut de Physique des 2 Infinis de Lyon (UMR5822), MATiCE
CNRS/Université Lyon 1
4, rue Enrico Fermi, F-69622 Villeurbanne Cedex (France)
[2] Université Lyon 1, IUT Lyon 1, département de chimie
1, rue l'émetteur, F-69622 Villeurbanne Cedex (France)
[3] Matériaux: Ingénierie et Science (UMR5510)
INSA Lyon
Campus LyonTech La Doua, 20 avenue Albert Einstein, F-69621 Villeurbanne cedex (France).
[4] CEMHTI (UPR3079)
CNRS Site Cyclotron, CS 30058, 3A rue de la Férollerie, F-45071 Orléans Cedex (France).

* Coresponding author : Dr. Nicolas BERERD ; n.bererd@ip2i.in2p3.fr

Keywords: electrochemical techniques; interface; 316L stainless steel; passive film; water radiolysis.

Abstract:

This work aims to study the effect of radiolytic species induced by water radiolysis on the passive behavior of 316L stainless steel. For this purpose, the stainless steel/neutral and aerated 0.02 M Na_2SO_4, electrolyte solution interface was irradiated with proton beams. A wide range of energies between 2 and 16 MeV was selected, varying the maximum of the energy deposition between 0.5 and 122 µm in water from the interface.
The irradiation experiments were performed at the CEMHTI cyclotron in Orléans and the 4 MV Van de Graaff accelerator at IP2I in Lyon (France). A dedicated irradiation device implemented with a 3-electrode cell dedicated to perform electrochemical measurements allows to measure the surface reactivity of the stainless steel as a function of the irradiation conditions. Results show that whatever the beam energy, the corrosion potential remains unchanged. It indicates that the very short-lived, highly reactive radiolytic species drive the corrosion potential and not only the recombination products such H_2O_2 or H_2. The stainless steel remains in the passive state whatever the irradiation conditions. However, it is shown that, during irradiation, the passive film is less protective. This evolution is attributed to radiolysis of bound water molecules in the passive film.

Introduction

In pressurized water reactor vessels, metallic materials such as austenitic steels, are subjected to multi-physical solicitations (irradiation, temperature, corrosion...). The coupling of these solicitations can induce accelerated damage [1-3] such as stress corrosion cracking (SCC) [4-15]. A significant stress can come from the tribological processes (sliding, fretting, impact...)[16], the corrosion induced by the contact between the steel and the primary liquid and the influence of the radiative environment of the reactor core.
Moreover, there is an indirect influence of irradiation on the evolution of the substrate. Damage effect on the steel is mainly due to neutron irradiation [17-19], but most of all, the chemical reactivity of the system is modified by the radical, ionic and/or molecular species, generated by the radiolysis of the primary liquid. The radiolysis process has already been widely studied by considering aqueous solutions [20]. The balance of pure water radiolysis is represented by the global reaction (R.1) [20-23]:

$$H_2O \xrightarrow{ionizing\ radiation} e^-_{aq}, HO^\bullet, H^\bullet, HO_2^\bullet, H_3O^+, OH^-, H_2O_2, H_2 \qquad (R.1)$$

Where e^-_{aq} is the hydrated, or solvated electron. This species, observed for the first time in the 60's [20], is described as an electron stabilized by a cluster formed with water molecules. More recently, this species has been extensively studied. Time-resolved studies mainly relied on Charge Transfer To Solvent (CTTS), using femtosecond UV laser pulses provide very important insights into the thermalization and solvation

of electrons. Complementary insights are obtained through multiphoton excitation of water at various central wavelengths. It can be assumed that the thermalized hydrated electron is now well characterized experimentally [24-27].
Three stages [20-23] classically describe the radiolysis of water, called respectively the physical (0 to 10^{-15} s after the passage of radiation), physicochemical (10^{-15} to 10^{-12} s) and chemical (10^{-12} to 10^{-6} s) stages. The values of the reaction kinetic constants are used to characterize the kinetics of the chemical dynamics of radiolysis. Many works compile them (for example [23, 28-31]). Globally, they vary from 10^7 to $2x10^{10}$ $L.mol^{-1}.s^{-1}$. R. S. Lillard *et al.* [32] point out that the lifetimes of many of these species are in the microsecond to nanosecond range.
In order to determine the role of radiolysis products in the reaction mechanisms of chemical transformations at the material surface, it is necessary to know the transport properties of the different formed species. A. J. Eliott [33], J. W. T. Spinks and R. J. Wood [21] have reported diffusion coefficient values close to a few 10^{-9} $m^2.s^{-1}$ for the principal radiolysis products from the literature. From these values, S. Moreau *et al.* [34] were able to estimate that the maximum distance traveled by the $HO^{\bullet}$ radical was of the order of 60 nm to 100 nm before being scavenged by the surface of a porous sample of Hastelloy or 316L stainless steel. Therefore, in the case of contact between a solid and an irradiated liquid, it is commonly accepted that radical products only play a role if they are produced very close to the interface. On the other hand, molecular products (H_2O_2 or H_2 if the latter remains in solution) can contribute to chemical transformations over longer distances.
In addition, in a study where water radiolysis is induced by gamma radiation, J.M. Joseph *et al.[35]* sought to demonstrate which reactions were most significant in establishing the steady state. They showed an important role of dissolved oxygen, the latter impacting the concentrations of radiolysis products. Similarly, pH also plays a role when it is below 5 and above 8. Between 5 and 8, the concentration of radiolysis products at steady state appears to be minimally affected. In aerated water, the concentrations of H_2O_2 and H_2 at steady state are higher than in the absence of oxygen. This increase in concentration occurs at the expense of the concentration of $HO^{\bullet}$ and solvated electrons. While these conclusions are very interesting, they were nevertheless obtained under gamma radiolysis. Moreover, the radical and molecular species modify the RedOx properties of the solution where they are produced. The impact of radiolysis on the evolution of solid/liquid interfaces is to date little studied and poorly known. Nevertheless, very interesting works have been carried out in confined environments. Energy transfers can take place between the solid and liquid phases, increasing or decreasing the production rates of radiolytic species [23, 34, 36-42]. The interface can be described as consisting of both superproduction sites and radiolysis product scavenge sites [34]. In particular, the role of surface hydroxyls is highlighted in several studies [23, 41]. By using porous solid samples with high specific surface area (porous silica, with controlled pore sizes ranging from 8 nm to 300 nm in diameter), it was observed an increase in the production of $HO^{\bullet}$ [38, 39, 42], e^-_{aq} [36-38, 43], H_2 [23, 36-38, 40, 41] and H_2O_2 [42] within the pores. The mechanisms proposed by the authors are essentially based on the transfer of energy from the solid to the liquid from the diffusion of a specific defect, the exciton, characterized in insulating or semiconductor materials [44]. The exciton can be self-trapped (STE for Self-Trapped Exciton), leading to the creation of highly distorted sites. STE could have several roles in the mechanisms of radiolytic species production. If the trapped electron still crosses the solid/liquid interface of the pores, it can induce the creation of the solvated electron, itself a precursor of H_2 [36, 37]. An alternative mechanism proposes that positive holes h^+ can also cross the interface to form $HO^{\bullet}$. These latter radicals are precursors of hydrogen peroxide, whose production is very dependent on the dose rate.
For metallic materials [34], the overproduction of $HO^{\bullet}$ at the interface can also be scavenged by the solid surface with yields depending on the metal itself. The passive film thickness of the 316L stainless steel is in the order of few nm which is considered too thin by the authors to modify the $HO^{\bullet}$ production rate. Three points of attention for corrosion studies are highlighted, among which one is particularly relevant in this paper: Can the $HO^{\bullet}$ radical reaction at the surface modify the transport within the passive layer or does it simply modify the redox potential of the solution?

Visual observation [45-48] of a 316L stainless steel and FeCrAl surfaces show clear differences depending on whether the area was irradiated and placed in contact with radiolysis products or only placed in contact with radiolysis products. These results seem to prove that radiolysis of water and irradiation of the material have coupled effects that impact the corrosion mechanisms of the materials.
In our previous work, we have demonstrated the ability of passivation of the 316L stainless steel under and after irradiation and under friction (tribocorrosion under irradiation) [49, 50] thanks to the original design of the experimental device. This device will be described again further. It allows altering the sample surface by applying a friction using an alumina pin. The radiolysis products are created near the stainless steel/aqueous solution interface. The evolution of the 316L surface reactivity is evaluated by measuring the corrosion potential, the polarization curves and by performing electrochemical impedance

spectroscopy (EIS) at corrosion potential. The analysis of electrochemical impedance diagrams using the Power Law Model (PLM) [51-53] allows us to obtain the resistivity profile in the passive film thickness, related to its physicochemical properties [54, 55].
In brief, the previous study [49, 50] has shown that:
(i) There exists a synergy between friction, irradiation, chemical evolution of the aqueous medium due to water radiolysis and corrosion of the stainless steel.
(ii) The value of the corrosion potential in the stationary state (*i.e.* in the presence of a passive layer) increases rapidly (within a few minutes) from the beginning of irradiation. The corrosion potential then remains constant during the whole irradiation and evolves again as soon as the proton beam is cut off. This second increase is not strictly identical for all samples.
(iii) The current density in the passive domain is enhanced under irradiation and radiolysis. This seems to show that the passive film is less protective during irradiation.
(iv) The nature of the passive film remains unchanged by irradiation and radiolysis. It is probably an oxyhydroxide. The film is commonly described [56] as a duplex structure composed by the inner layer (mainly of Cr_2O_3) and the outer oxyhydroxide layer enriched in iron and chromium. On the other hand, the determination of the passive film thickness using the PLM allows us to state the hypothesis that under irradiation and under radiolysis, the outer layer becomes thicker while the inner layer thickness becomes thinner. The protective properties of the stainless-steel passive film then evolve, as they are directly related to the presence of the Cr_2O_3 layers.

The objective of the present paper is to further understand the role of radiolysis at the 316L/solution interface, particularly the role of radical species on passive properties of the stainless steel. The results were obtained without friction, using the same experimental set-up (see *Supporting information*). Irradiation experiments were performed with a proton beam produced by the cyclotron at CEMHTI (CNRS, Orléans, France) or by the 4 MV Van de Graaff accelerator at IP2I (CNRS/University Lyon 1, Villeurbanne, France). The advantage of ion beams is that the position of the maximum energy deposition can be precisely controlled. In this study, the energy deposition, and thus the production of radiolysis products, is performed close to the sample surface in order to study its impact on chemical phenomena occurring at the interface.

Results and Discussion

Irradiation conditions are explained in detail in the *Supporting Materials* section. Here are the highlights. Two configurations of irradiation conditions were used. In both cases, solutions are irradiated in aerated conditions at a pH equal to 6. In the first configuration, 500 µm-thick samples were irradiated with 16 MeV protons at 10 nA for one hour. Under these conditions, the protons have an average kinetic energy equal to (2.7 ± 0.5) MeV at the steel/electrolyte interface. The protons travel an average distance in water, denoted R_w, equal to (122 ± 43) µm if the uncertainty of the sample thickness is neglected. These irradiation conditions will be referred to as Reference Conditions in the remainder of this paper. The second configuration will be referred to in the remainder of this article as IP2I irradiations. 30 µm thick samples were irradiated with 2.0, 2.2, 2.7, 2.8 and 3.0 MeV protons. At the first two energies, the protons did not penetrate the steel foil. For energies between 2.7 and 3.0 MeV, protons penetrate the solution at average distances between (0.5 ± 1.7) and (22.0 ± 3.7) µm. The evolution of the solid/electrolyte interface was monitored using electrochemical techniques: corrosion potential measurement, polarization curve and electrochemical impedance spectroscopy. Finally, proton beam-induced damage to the 316L steel samples was negligible (see Supporting Materials section).

Evolution of the corrosion potential of the 316L stainless steel in irradiated solution

Under these irradiation conditions, the energy deposition in the electrolyte near the interface varies for each incident energy (see *Supporting Materials*), and consequently so does the amount of formed radiolysis products. The value of the corrosion potential of 316L steel is expected to be different for each experiment. **Figure 1** shows the evolution of the corrosion potential for the different proton energies.
Results plotted in ***Figure 1a*** were obtained using the reference experimental conditions. The corrosion potential value in the presence of a passive layer increases rapidly from the start of the irradiation until a plateau is reached. Then, it evolves again as soon as the proton beam is cut off, towards a nobler potential before stabilizing and then slowly decreasing. This curve has the same shape as the one described in the introduction, published in [49].

Figure 1b shows two different evolutions depending on whether the protons pass through (2.7 MeV to 3 MeV) or are stopped in the sample (2.0 and 2.2 MeV). After a rapid increase of the corrosion potential, the potential increases very slightly as a function of time, in contrast to the reference experiment which exhibits a plateau. This slight increase may be related either to the temperature increase of the sample during the energy deposition or to a slight irradiation effect as observed by P. L. Airey during irradiation by gammas or by electrons in an acid medium on platinum [57, 58]. In all cases, these two experiments show the observed potential differences are indeed linked to the aqueous solution irradiation (*i.e.* to the radiolysis of the water) and not to the irradiation of the sample. Let's recall that with accelerated protons, energy deposition traces in water overlap starting from a LET of 20 keV/µm[59], which is the case in our experiments (see Table S.1 in *Supporting Materials* section). This overlap increases the molecular radiolysis product yield (H_2, H_2O_2). The yields of radical radiolysis products decrease with increasing LET, except for the $HO_2^{\bullet}$ radical, which sees its yield increase. At the pH of our experiments, the $HO_2^{\bullet}$ radical exists predominantly in its $O_2^{\bullet -}$ form [60].

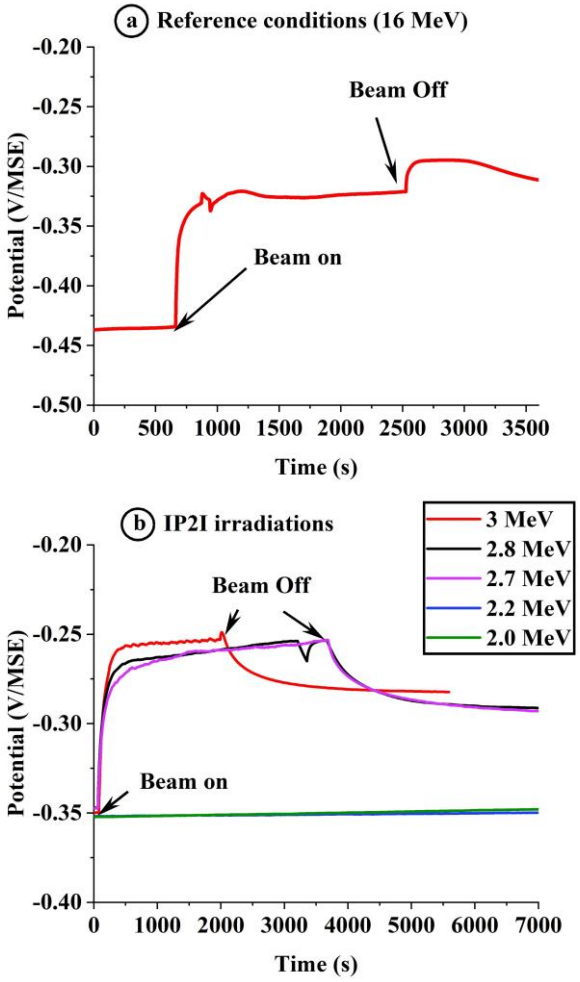

Figure 1: Corrosion potential evolution for (a) reference irradiation conditions and (b) IP2I irradiation conditions. The error bar is estimated to 0.01 V.

Between 2.7 MeV and 3.0 MeV, when protons cause radiolysis of the aqueous solution, the potential increase is always observed ($\Delta E \approx +0.1$ V). The slight potential increase equal to 0.01 V observed between 2.8 and 3 MeV is within the error bar of 0.01 V and is therefore not significant. These results confirm those already obtained in the literature, such as for example, by R. S. Glass *et al.* [61] and G. P. Marsh *et al.* [62] under gamma irradiation or by other authors under proton irradiation [45, 63, 64]. E. Leoni *et al.* [63] attributed the potential increase to the presence of hydrogen peroxide, which is a metastable radiolysis product in solution, as well as to the $HO^{\bullet}$ radical. More recently, with a proton beam of 6 or 22 MeV kinetic energy (at the interface) and in an aqueous solution representative of the primary liquid under high pressure and high temperature, B. Muzeau *et al.* [64] and M. Wang *et al.* [45] also observe an increase in the potential of the stainless steel under irradiation. This increase depends on the

temperature and the irradiation dose. They also note that the presence of dissolved H_2, added before irradiation, decreases the oxidizing effect of water radiolysis. Finally, E. Leoni *et al.* [63] showed that for stainless steels under irradiation (6 MeV protons at the solution/sample interface; aerated or deaerated solutions), the O_2, H_2O_2, HO_2^-, $HO^\bullet$, $HO_2^\bullet$ and $O_2^{\bullet-}$ species have oxidizing properties. It can be noted that the short-lived radiolytic species (lifetime lower than 1 µs) can only play a role at the interface considering their diffusion coefficients displayed in ***Table 1***. The 3D diffusion radii have been estimated for each radical species considering a lifetime of radicals of up to 1 µs. This time corresponds to the order of magnitude of the end of the chemical stage of radiolysis. It should be noticed that the irradiation parameters of our reference conditions are close to those used by E. Leoni *et al.* and M. Wang *et al.*

Table 1 : Diffusion coefficients D of the main radiolysis products in water at 25 °C, compiled from [21, 33]. Dr is the 3D diffusion radii for radical species, calculated using Dr = $\sqrt{6.D.t}$, where t is equal to 1 µs.

Species	D (10^{-9} m²/s)	Ref.	Dr (µm)	Species	D(10^{-9} m²/s)	Ref.	Dr (µm)
e^-_{aq}	4.9 4.5 4.82	[21] [65, 66] [67]	0.17 0.16 0.17	O_2	2.1 2 2.4	[65] [66] [67]	
$H^\bullet$	7 7	[65, 66] [67, 68]	0.20 0.20	H_2O_2	2.2 1.4 2.3	[65, 66] [69] [67]	
$HO^\bullet$	2.3 2.8 2.2	[21] [65, 66] [67, 70]	0.120.13 0.11	H^+	9.0 9.3	[65, 66] [67]	
$O_2^{\bullet-}$	1.5 2.1 4.82	[21] [65, 66] [70]	0.09 0.11 0.17	OH^-	5 5.3	[65, 66] [67]	
H_2	5 4.8	[65, 66] [70]		$HO_2^\bullet$	2 1.4 2.3	[65, 66] [69] [70]	0.11 0.09 0.12
HO_2^-	2	[59, 60]	0.11				

When the 3 MeV irradiation is stopped, a smaller second potential increase is visible (**Figure 1b**) in contrast with the reference conditions (**Figure 1a**) where a more significant increase is observed. This electrochemical behavior has also been observed, or even guessed, by other authors [61, 63, 64], without being discussed. We assume it is related to the consumption of short-lived radiolysis products (e^-_{aq}, $H^\bullet$, $HO^\bullet$, $O_2^{\bullet-}$). The evolution of corrosion potential towards more anodic values, could be attributed to the stopping of the production of radiolytic reducing species (H_2 and e^-_{aq}). Further experiments and modeling are necessary to confirm this hypothesis.

The role of H_2 on the corrosion potential of stainless steels has been discussed in the literature. During irradiation, H_2 can play a more or less key role, according to the authors. R. S. Glass *et al.* [61] have shown that H_2 had a weak influence on the potential value of 316L or 304L stainless steels placed in contact with a hydrogenated solution and in the presence of hydrogen peroxide. They attribute this result to the low dissociation rate of H_2 on the sample surface, implying a weak electrochemical response compared to that of H_2O_2. The authors cannot conclude on the role of $H^\bullet$, which refers to one of the three points of attention stated by S. Moreau *et al.* [34]. R. S. Glass *et al.* do not mention the solvated electron. M. Wang *et al.* [45] also observe the influence of H_2 by showing a less marked oxidizing response at 300 °C with a higher pressure of dissolved dihydrogen than at lower pressure. Moreover, R. S. Lillard *et al.* [32, 71] highlight the role of dihydrogen on the corrosion of Inconel, 304L and 316L stainless steels, tungsten, gold and tantalum during irradiation by 800 MeV protons. Indeed, for stainless steel samples, the corrosion rates are lower with dissolved dihydrogen than without. On the other hand, for other metals, such as gold, no effect is shown.
Moreover, in the literature, E. Leoni *et al.*[63] use the Na_2SO_4 electrolyte for their radiolysis study at the interface with steel, without specifying the role of SO_4^{2-} radiolysis. Nevertheless, P. Bouniol *et al.* studied

the radical sulfur radiolysis in cementitious matrices containing sulfides[72]. Sulfur chemistry is diverse, with oxidation states ranging from - II to +VI and numerous species sensitive to pH. The sulfate ion and its sulfur at the +VI oxidation state are no longer susceptible to oxidation. However, they are likely sensitive to reduction by certain radical species depending on the chemistry and radiation conditions. Furthermore, the Na_2SO_4 concentration of 0.02 M is significant enough to impact radiolysis mechanisms and deserve further investigations.

In conclusion, **Figure 1** demonstrates the influence of water radiolysis on the corrosion potential of 316L stainless steel. The passivation seems to be favored, which is highlighted by the potential increase to more anodic values. The second potential difference observed when the irradiation is stopped shows the establishment of a new stationary state related to the consumption of short-lived radiolysis products. From the point of view of the interface, it is important to note that the variation of the proton energy deposition (and thus of the Bragg peak – interface distance), even small, does not change the values of the obtained potential. It seems therefore that the phenomena taking place at the solid/liquid interface are predominant in the establishment of the stationary state obtained when the solution is radiolysed.
Thus, two questions may arise from these results:
(i) Does the stainless steel remain passivated during irradiation?
(ii) Does the system change from the passive to the transpassive regime as observed by P. Wang *et al.*[48] in their study on the corrosion of FeCrAl alloys in hydrogenated water? The latter study is based on the theoretical evaluation of the system potential value, putting it into perspective in the Pourbaix diagrams of Fe and Cr, calculated at 300 °C. These results were obtained at high temperature and high pressure and complement those obtained by S.S. Raiman *et al.* [46, 47] and R. D. Hanbury *et al.* [73] on 316L stainless steel. All these authors have characterized a thick oxide layer at the surface composed by an inner oxide rich in Cr (Cr spinel layer, rich in Fe and Ni) acting as a barrier to oxygen diffusion and an outer iron oxide (magnetite or hematite depending on the potential). The role of radiolysis of the solution, with a composition close to that of the primary liquid of a PWR or BWR, seems to facilitate the dissolution of Cr from the inner oxide.

The following section aims to answer these questions.

Global kinetic and thermodynamic approach of the system

As a reminder, the passive film is a duplex oxide consisting of a chromium oxide rich layer in contact with the metal and of a mixture of iron oxide and hydroxide in contact with the solution. Nevertheless, as written by S. Marcelin *et al.* [54], the passivation ability of metallic materials is governed by the kinetic formation of the passive films and their physicochemical properties that allow their maintenance conditions [74]. It is therefore necessary to complete the thermodynamic approach with a kinetic vision of the system. C. Boissy *et al.* [74] and B. Normand *et al.* [75] point out the interest of polarization curves to obtain information about the passivation ability of the materials and the range of existence of the passive film. **Figure 2** shows the polarization curves obtained under reference conditions (cathodic and anodic branches are obtained consecutively).

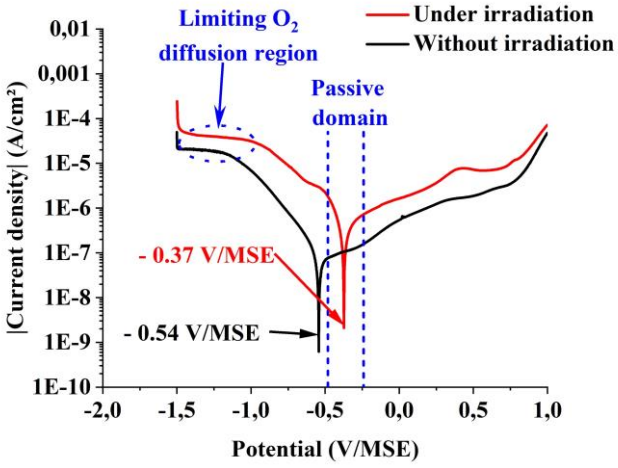

Figure 2: Polarization curves obtained for the 316L stainless steel in contact with a Na_2SO_4 solution, 0.02 M. In black, the results obtained without irradiation, in red, the results obtained under proton irradiation in the reference conditions. MSE: Mercury-mercurous sulfate Electrode, sweep rate = 1 mV/s

This figure firstly allows us to determine the values of the corrosion potential for the two conditions: - 0.54 V/MSE (+ 0.11 V/SHE) without irradiation and - 0.37 V/MSE (+ 0.28 V/SHE) under irradiation. The potential difference measured in **Figure 2** is equal to ΔE = + 0.17 V. It is of the same order of magnitude as in **Figure 1a**. However, the measurements were performed on a different sample, which may account for the observed discrepancy. In addition, the shape of the curve provides information about the passivity of the surface of the 316L stainless steel. The passive domain is clearly defined on the anodic curves obtained without irradiation (black curve). The end of the passive plateau can be placed at about - 0.24 V/MSE (+ 0.41 V/SHE). Under irradiation, the corrosion potential is located within the passive plateau, even if it is close to the beginning of the transpassive domain. From a purely kinetic point of view, as previously published [49], it is important to note the difference in current density between the polarization curve obtained under irradiation and that obtained without irradiation. Maintaining the passive film therefore induces greater dissolution of the material under irradiation that could confirm the presence of defects or thinning of passive film.
From a purely thermodynamic point of view, the Pourbaix diagrams [76] (***Figure 3***) confirm these observations. The potential difference □E = + 0.17 V is noted by the blue arrow in the figure for a pH equal to 6. As expected, there is no change of domain neither for the Pourbaix diagram of Fe, nor that of Cr.
In conclusion, under the reference irradiation conditions, the stainless steel remains in the passive domain. Nevertheless, the difference in passive film sustaining current with and without irradiation may suggest an evolution of the passive film under irradiation. This point will be discussed in the next section.

Behavior of the passive film under irradiation

Figure 4a shows the impedance modulus and the phase angle as a function of frequency. The experimental data have been corrected by electrolyte resistance to highlight the dependence of phase on frequency [53]. The measurements under irradiation and after irradiation were repeated respectively 3 and 4 times and we observed a very good reproducibility.
The impedance diagrams are characterized by two-time constants. The low frequency time constant is attributed to the charge transfer at the passive film/electrolyte interface and the high frequency time constant is attributed to the response of the passive film. According to the literature, the passive film is thicker under irradiation [49, 55]. This increase in thickness is reversible as soon as the irradiation is stopped. We have assumed from [77, 78] that the thinner the film, the more protective it is. Under irradiation, the passive film may be less protective since it is more defective [49, 54]. Indeed, under irradiation, the thickness of the chromium oxide layer clearly decreases, a link can be made with the results of S. S. Raiman, R. D. Hanbury and P. Wang *et al.* [46-48, 73] recalled above.

The low frequency evolution of the spectra in **Figure 4a** is not yet explained. To better understand this evolution, spectra were acquired without irradiation at cathodic potential (**Figure 4b**), from the corrosion potential of the sample (-0.4 V/MSE) to the oxygen diffusion plateau (-1.1 V/MSE) (see the blue dashed part of the polarization curve **Figure 2**). This plateau is observed because the diffusion of dissolved oxygen in the solution limits the reaction rates. For the last potential (blue curve, - 1.1 V/MSE), the passive film is reduced (**Figure 2**). It is striking to note that, at low frequency and for this potential, the evolution of the phase as a function of time (**Figure 4b**) has the same shape as the evolution of the phase acquired under irradiation (red curve, **Figure 4a**). However, the spectrum obtained without irradiation is characteristic of a reduced passive film whereas, under irradiation and reference conditions, and based on the polarization curve (**Figure 2**), the material should be passivated. It should be mentioned that the high radioactivity of stainless-steel samples at the end of irradiation under reference conditions prevents *post-mortem* characterizations of the passive layer. Nevertheless, the existence of the passive layer can be demonstrated by monitoring the corrosion potential under tribological conditions and under irradiation.
Figure 5 shows the evolution of the corrosion potential of a stainless steel sample placed in contact with the electrolyte

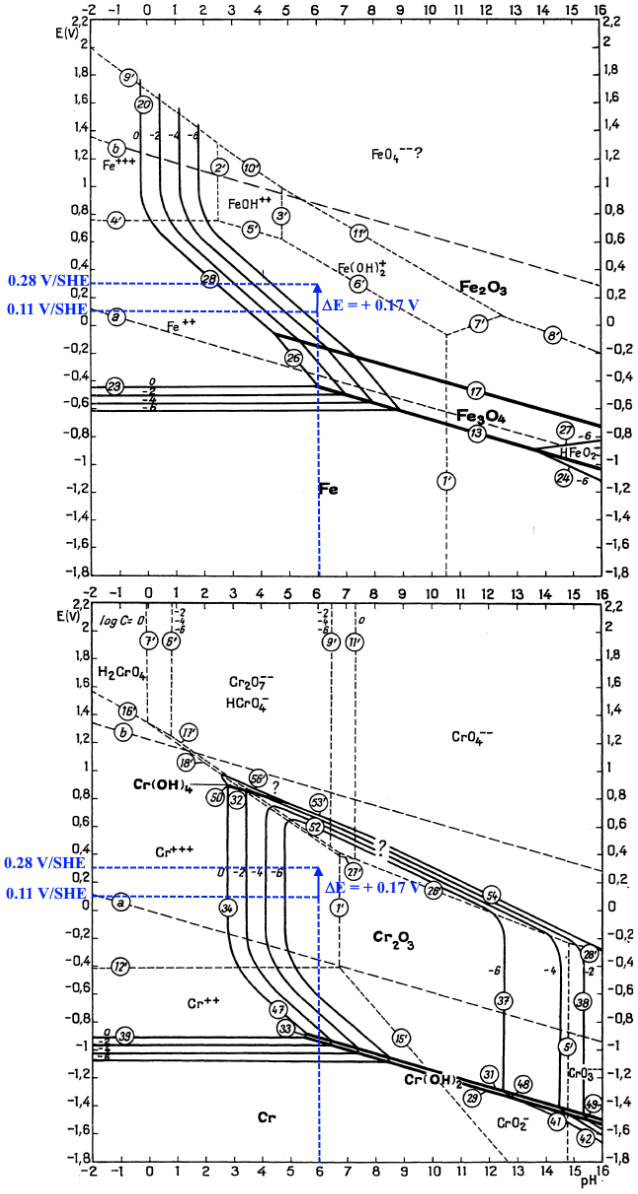

Figure 3: Pourbaix diagrams [76] at 25 °C a) of iron and b) of chromium The blue arrow represents on both diagrams the potential difference ΔE = + 0.17 V. (SHE: Standard Hydrogen Electrode). Reprinted with permission from AMPP from "Atlas of Electrochemical Equilibria in Aqueous Solutions", M. Pourbaix, 1974.

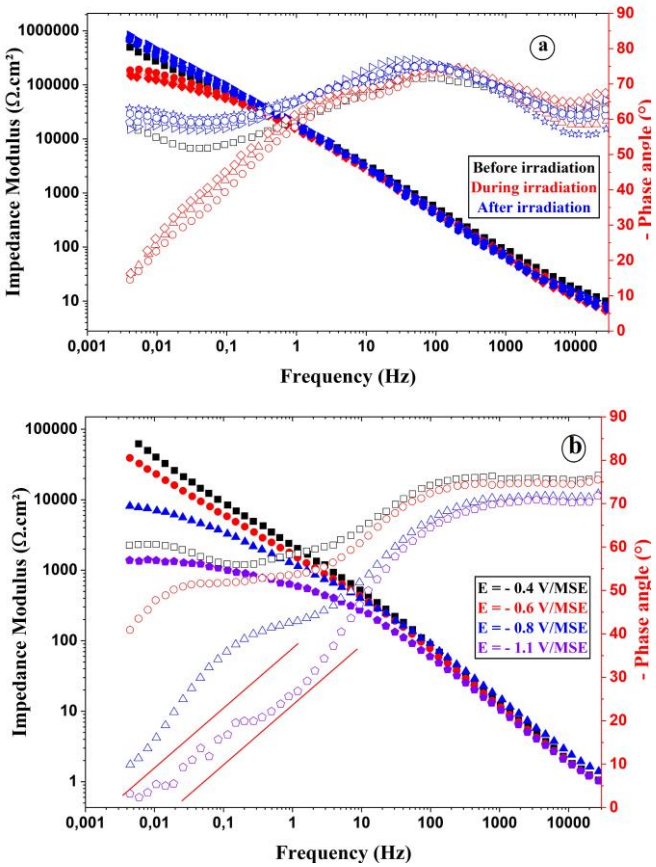

Figure 4: a) Electrochemical impedance diagrams in Bode coordinates obtained: (a) before, during and after irradiation under reference conditions and at corrosion potential and b) without irradiation obtained in the cathodic domain from - 0.4 V/MSE (corrosion potential of this sample) to -1.4 V/MSE (potential located in the limiting O_2 diffusion region). The full symbols are related to modulus values and the empty ones are related to the phase values. The red lines are used to guide the eye.

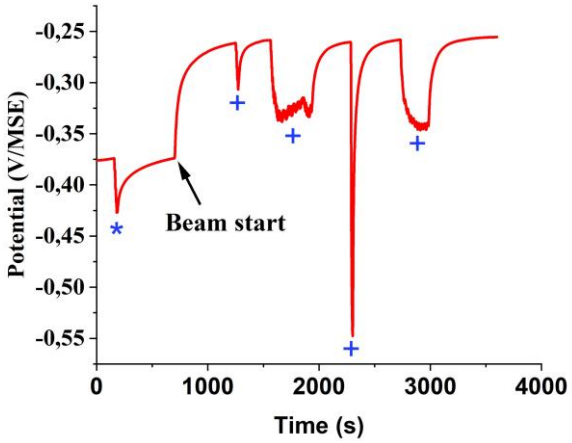

Figure 5: Evolution of corrosion potential for a 316L stainless sample in contact with a non-irradiated and then irradiated Na_2SO_4 solution (preliminary result). The transient spotted by * corresponds to the depassivation/repassivation of the surface without irradiation and the transients spotted by + corresponds to the depassivation/repassivation of the surface during irradiation under reference conditions.

This curve is a preliminary result of the tribocorrosion studies under irradiation of 316L steel. After the sample preparation protocol, the corrosion potential value tends to -0.37 V/MSE. Following a back-and-

forth movement of the alumina pin on the sample surface, a potential transient is observed (spotted by * in ***Figure 5***). Following the passive film stripping, the metal comes in contact with the solution, which results in a sudden drop in potential. Then, the surface repassivates, and the film is reconstructed as already observed in other studies [49, 79, 80]. The potential then recovers its initial value. At $t \approx 600$ s, the irradiation in the reference conditions starts, leading to a potential difference. The stationary state is reached for a potential value of about - 0.25 V/MSE. From $t \approx 1250$ s, the pin moves back and forth on the surface of the sample. Potential transients are observed (spotted by + in ***Figure 5***). The existence of these transients is the signature of the stainless steel repassivation.
If the presence of a passive film under irradiation in the reference conditions is well observed, the electrochemical impedance spectra make it possible to assert that the passive film is degraded and made up of a weak protective layer of chromium oxide [49, 50, 54]. The radiolysis of the aqueous solution plays a role in the evolution of the passive film under irradiation. It is then logical to wonder whether the radiolysis products play a role in the first layers of solution in contact with the stainless steel or in the passive film itself by the radiolysis of bound water in the passive film, as described by G. Okamoto [81]. Indeed, this author underlines that the most important parameter for controlling the corrosion resistance of steel is the amorphous nature of the film in which bound water is included. Bound water could be compared to water confined in porous solids which has been the subject of several studies [34, 36-42]. These results allow us to propose the hypothesis that chemical transformations under radiolysis take place in the passive film and not only in the first layers of water adsorbed on the sample.

Conclusion

The aim of this work was to specify the role of radiolysis of water at the solid/solution interface. It is a first step in the understanding of tribocorrosion of stainless steel under irradiation in contact with a liquid also irradiated. The irradiation device used in this work allowed to irradiate an aqueous solution as close as possible to the water/steel interface. By varying the proton energy, the maximum of the Bragg peak could be placed at different distances from the interface. This variation did not lead to a variation of the electrochemical potential difference of the system.
The results show that:

(i) the radiolytic phenomena taking place at the solid/liquid interface are predominant in the establishment of the stationary state obtained when the solution is radiolysed. The short-lived radiolysis products seem to participate in the establishment of the stationary state observed under irradiation.

(ii) This system driven by the kinetics of the passive film formation and its physico-chemistry under irradiation does not evolve towards the transpassive regime but remains in the passive domain.

(iii) A passive film does remain under irradiation. The latter displaying a thinner chromium oxide layer shows degraded properties under irradiation. Radiolysis of the bound water in the passive film seems to play an important role during the passivation of stainless steel under irradiation.

In the perspective of this work, it will be necessary to study the chemical mechanisms occurring at the interface, for example by using pulsed beams.

Supporting Information

The authors have cited additional references within the Supporting Information. [46, 47, 49, 50, 53, 64, 73, 82-84]

Acknowledgements

This project received financial support from the CNRS through the NEEDS program and through the MITI interdisciplinary programs.
The authors gratefully acknowledge the support of the French EMIR&A network (FR CNRS 3618) on the CEMHTI platform.
The authors would like to thank the accelerator teams from CEMHTI and IP2I laboratories for their help in the irradiation experiments. They are also grateful to M. Fucina and A. Eroutine for their fruitful contributions during their internship. The authors also thank S. Flores for her help with bibliographic research and B. Muzeau for insightful discussion on the impact of irradiation on the electrolyte evolution. They also thank B. Farizon for his valuable advice.

1. Feron, D., E. Herms, and B. Tanguy, *Behavior of stainless steels in pressurized water reactor primary circuits.* Journal of Nuclear Materials, 2012. **427**(1-3): p. 364-377.
2. Tanguy, B., *Corrosion sous contrainte assistée par l'irradiation des aciers inoxydables austénitiques (IASCC).* Revue de Métallurgie, 2011. **108**: p. 39-46.
3. Tanguy, B., F. Sefta, and P. Joly, *Le vieillissement des Internes de Cuve -Programme de recherche en support à la durée de fonctionnement des réacteurs REP.* Revue Generale Nucleaire, 2015. **3**(3): p. 56-63.
4. Lillard, R.S. and B.A. Pint, *Principles of Corrosion in Nuclear Systems: Theory and Analytical Methods*, in *Comprehensive Nuclear Materials, 2nd edition*, R.J.M. Konings and R.E. Stoller, Editors. 2020. p. 1-32.
5. Ehrnstén, U., *Corrosion and Stress Corrosion Cracking of Austenitic Stainless Steels*, in *Comprehensive Nuclear Materials, 2nd edition*, R.J.M. Konings and R.E. Stoller, Editors. 2020, Elsevier BV. p. 118-128.
6. Andresen, P.L. and G.S. Was, *Irradiation Assisted Stress Corrosion Cracking*, in *Comprehensive Nuclear Materials*, R.J.M. Konings and R.E. Stoller, Editors. 2019, Elsevier BV. p. 190-217.
7. Was, G.S., Y. Ashida, and P.L. Andresen, *Irradiation-assisted stress corrosion cracking.* Corrosion Reviews, 2011. **29**(1-2): p. 7-49.
8. Shoji, T., S. Suzuki, and K.S. Raja, *Current status and future of IASCC research.* Journal of Nuclear Materials, 1998. **258**: p. 241-251.
9. Bruemmer, S.M., E.P. Simonen, P.M. Scott, P.L. Andresen, G.S. Was, and J.L. Nelson, *Radiation-induced material changes and susceptibility to intergranular failure of light-water-reactor core internals.* Journal of Nuclear Materials, 1999. **274**(3): p. 299-314.
10. Chopra, O.K. and A.S. Rao, *A review of irradiation effects on LWR core internal materials - IASCC susceptibility and crack growth rates of austenitic stainless steels.* Journal of Nuclear Materials, 2011. **409**(3): p. 235-256.
11. Fournier, L., M. Savoie, and D. Delafosse, *Influence of localized deformation on A-286 austenitic stainless steel stress corrosion cracking in PWR primary water.* Journal of Nuclear Materials, 2007. **366**(1-2): p. 187-197.
12. Scott, P., *A review of irradiation assisted stress-corrosion cracking.* Journal of Nuclear Materials, 1994. **211**(2): p. 101-122.
13. McNeil, M.B., *Irradiation assisted stress corrosion cracking.* Nuclear Engineering and Design, 1998. **181**(1-3): p. 55-60.
14. Jiao, Z. and G.S. Was, *Impact of localized deformation on IASCC in austenitic stainless steels.* Journal of Nuclear Materials, 2011. **408**(3): p. 246-256.
15. *Stress Corrosion Cracking in Light Water Reactors: Good Practices and Lessons Learned*. Vol. 43(1). 2011, International Atomic Energy Agency (IAEA): IAEA.
16. Landolt, D., S. Mischler, and M. Stemp, *Electrochemical methods in tribocorrosion: a critical appraisal.* Electrochimica Acta, 2001. **46**(24-25): p. 3913-3929.
17. Hashimoto, N., R. Kasada, B. Raj, and M. Vijayalakshmi, *Radiation Effects in Ferritic Steels and Advanced Ferritic-Martensitic Steels*, in *Comprehensive Nuclear Materials, 2nd edition*, R.J.M. Konings and R.E. Stoller, Editors. 2020, Elsevier B.V. p. 226-254.
18. Garner, F.A., *Radiation-Induced Damage in Austenitic Structural Steels Used in Nuclear Reactors*, in *Comprehensive Nuclear Materials - 2nd edition*, R.J.M. Konings and R.E. Stoller, Editors. 2020, Elsevier B.V. p. 57-168.
19. English, C. and J. Hyde, *Radiation Damage of Reactor Pressure Vessel Steels*, in *Comprehensive Nuclear Materials, 2nd edition*, R.J.M. Konings and R.E. Stoller, Editors. 2012, Elsevier BV. p. 169-196.
20. Ferradini, C. and J.P. Jay-Gerin, *Radiolysis of water and aqueous solutions - History and present state of the science.* Canadian Journal of Chemistry, 1999. **77**(9): p. 1542-1575.
21. Spinks, J.W.T. and R.J. Woods, *An Introduction to Radiation Chemistry, 3rd edition*. 1990.
22. Farhataziz and M.A.J. Rodgers, *Radiation Chemistry: Principles and Applications*. 1987: Vch Pub.
23. Le Caër, S., *Water Radiolysis: Influence of Oxide Surfaces on H_2 Production under Ionizing Radiation.* Water, 2011. **3**: p. 235-253.
24. Yamamoto, Y.I. and T. Suzuki, *Ultrafast Dynamics of Water Radiolysis: Hydrated Electron Formation, Solvation, Recombination, and Scavenging.* Journal of Physical Chemistry Letters, 2020. **11**(14): p. 5510-5516.
25. Svoboda, V., R. Michiels, A.C. LaForge, J. Med, F. Stienkemeier, P. Slavícek, and H.J. Wörner, *Real-time observation of water radiolysis and hydrated electron formation induced by extreme-ultraviolet pulses.* Science Advances, 2020. **6**(3).
26. Renault, J.P. and S. Pommeret, *Seeing the solvated electron in action: First-principles molecular dynamics of NO3- and N2O reduction.* Radiation Physics and Chemistry, 2022. **190**: p. 109810.
27. Novelli, F., K.X. Chen, A. Buchmann, T. Ockelmann, C. Hoberg, T. Head-Gordon, and M. Havenith, *The birth and evolution of solvated electrons in the water.* Proceedings of the National Academy of Sciences of the United States of America, 2023. **120**(8).
28. Burns, W.G. and P.B. Moore, *Water radiolysis and its effect upon in-reactor zircaloy corrosion.* Radiation Effects and Defects in Solids, 1976. **30**(4): p. 233-242.
29. Elliot, A.J. and D.M. Bartels, *The reaction set, rate constants and g-values for the simulation of the radiolysis of light water over the range 20 deg to 350 deg C based on information available in 2008*. 2009, Canada: AECL, AECL-153-127160-450-001. 162.
30. Buxton, G.V., C.L. Greenstock, W.P. Helman, and A.B. Ross, *Critical-review of rate constants for reactions of hydrated electrons, hydrogen-atoms and hydroxyl radicals (OH/.O-) in aqueous-solution.* Journal of Physical and Chemical Reference Data, 1988. **17**(2): p. 513-886.
31. Bouniol, P., *State of knowledge on the water radiolysis in cemented wasteforms and its approach by simulation*. 2004, France: CEA, CEA-R--6069. 143.
32. Lillard, R.S., D.L. Pile, and D.P. Butt, *The corrosion of materials in water irradiated by 800 MeV protons.* Journal of Nuclear Materials, 2000. **278**(2-3): p. 277-289.
33. Elliot, A.J., *Rate Constants and G-Values for the Simulation of the Radiolysis of Light Water over the Range 0-300°C*. 1994, Canada: AECL, AECL-11073, COG-94-167. 61.
34. Moreau, S., M. Fenart, and J.P. Renault, *Radiolysis of water in the vicinity of passive surfaces.* Corrosion Science, 2014. **83**: p. 255-260.
35. Joseph, J.M., B.S. Choi, P. Yakabuskie, and J.C. Wren, *A combined experimental and model analysis on the effect of pH and O₂(aq) on γ-radiolytically produced H₂ and H₂O₂.* Radiation Physics and Chemistry, 2008. **77**(9): p. 1009-1020.
36. Musat, R.M., A.R. Cook, J.P. Renault, and R.A. Crowell, *Nanosecond Pulse Radiolysis of Nanoconfined Water.* Journal of Physical Chemistry C, 2012. **116**(24): p. 13104-13110.
37. Musat, R., G. Vigneron, D. Garzella, S. LeCaer, J.F. Hergott, J.P. Renault, and S. Pommeret, *Water reduction by photoexcited silica and alumina.* Chemical Communications, 2010. **46**(14): p. 2394-2396.
38. Musat, R., S. Moreau, F. Poidevin, M.H. Mathon, S. Pommeret, and J.P. Renault, *Radiolysis of water in nanoporous gold.* Physical Chemistry Chemical Physics, 2010. **12**(39): p. 12868-12874.
39. Foley, S., P. Rotureau, S. Pin, G. Baldacchino, J.P. Renault, and J.C. Mialocq, *Radiolysis of confined water: Production and reactivity of hydroxyl radicals.* Angewandte Chemie-International Edition, 2005. **44**(1): p. 110-112.

40. Rotureau, P., J.P. Renault, B. Lebeau, J. Patarin, and J.C. Mialocq, *Radiolysis of confined water: Molecular hydrogen formation.* Chemphyschem, 2005. **6**(7): p. 1316-1323.
41. Le Caer, S., P. Rotureau, F. Brunet, T. Charpentier, G. Blain, J.P. Renault, and J.C. Mialocq, *Radiolysis of confined water: Hydrogen production at a high dose rate.* Chemphyschem, 2005. **6**(12): p. 2585-2596.
42. Le Caer, S., J.P. Renault, and J.C. Mialocq, *Hydrogen peroxide formation in the radiolysis of hydrated nanoporous glasses: A low and high dose rate study.* Chemical Physics Letters, 2007. **450**(1-3): p. 91-95.
43. Musat, R., *Dynamique et réactivité dans l'eau confinée*, in *Chimie*. 2008, Thèse de l'université Paris XI.
44. Petrik, N.G., A.B. Alexandrov, and A.I. Vall, *Interfacial energy transfer during gamma radiolysis of water on the surface of ZrO_2 and some other oxides.* Journal of Physical Chemistry B, 2001. **105**(25): p. 5935-5944.
45. Wang, M., S. Perrin, C. Corbel, and D. Féron, *Electrochemical behaviour of 316L stainless steel exposed to representative chemistry in pressurised water reactors under proton radiation.* Journal of Electroanalytical Chemistry, 2015. **737**: p. 141-149.
46. Raiman, S.S. and G.S. Was, *Accelerated corrosion and oxide dissolution in 316L stainless steel irradiated in situ in high temperature water.* Journal of Nuclear Materials, 2017. **493**: p. 207-218.
47. Raiman, S.S., D.M. Bartels, and G.S. Was, *Radiolysis driven changes to oxide stability during irradiation-corrosion of 316L stainless steel in high temperature water.* Journal of Nuclear Materials, 2017. **493**: p. 40-52.
48. Wang, P., S. Grdanovska, D.M. Bartels, and G.S. Was, *Effect of radiation damage and water radiolysis on corrosion of FeCrAl alloys in hydrogenated water.* Journal of Nuclear Materials, 2020. **533**.
49. Normand, B., N. Bererd, P. Martinet, S. Marcelin, M. Moine, J. Feirrera, D. Baux, T. Sauvage, and N. Moncoffre, *Electrochemical behaviour of austenitic stainless steel under tribological stresses and irradiation.* Corrosion Science, 2020. **176**: p. 108945.
50. Martinet, P., *Effects of proton-induced radiolysis at interfaces: Application to the case of stainless steel in Na_2SO_4 medium*. 2021, PhD thesis, University Claude Bernard Lyon 1.
51. Hirschorn, B., M.E. Orazem, B. Tribollet, V. Vivier, I. Frateur, and M. Musiani, *Constant-Phase-Element Behavior Caused by Resistivity Distributions in Films I. Theory.* Journal of the Electrochemical Society, 2010. **157**(12): p. C452-C457.
52. Hirschorn, B., M.E. Orazem, B. Tribollet, V. Vivier, I. Frateur, and M. Musiani, *Constant-Phase-Element Behavior Caused by Resistivity Distributions in Films II. Applications.* Journal of the Electrochemical Society, 2010. **157**(12): p. C458-C463.
53. Orazem, M.E., N. Pebere, and B. Tribollet, *Enhanced graphical representation of electrochemical impedance data.* Journal of the Electrochemical Society, 2006. **153**(4): p. B129-B136.
54. Marcelin, S., Z. Zhang, B. Ter-Ovanessian, and B. Normand, *Relationship between the Resistivity Profiles Obtained from the Power Law Model and the Physico-Chemical Properties of Passive Films.* Journal of the Electrochemical Society, 2021. **168**(2): p. 021503.
55. Marcelin, S., B. Ter-Ovanessian, and B. Normand, *Electronic properties of passive films from the multi-frequency Mott-Schottky and power-law coupled approach.* Electrochemistry Communications, 2016. **66**: p. 62-65.
56. Wang, Z.C., A. Seyeux, S. Zanna, V. Maurice, and P. Marcus, *Chloride-induced alterations of the passive film on 316L stainless steel and blocking effect of pre-passivation.* Electrochimica Acta, 2020. **329**: p. 135159.
57. Airey, P.L., *Effect of irradiation on electrode processes .1. hydrogen electrode in dilute-solutions.* Journal of the Chemical Society-Faraday Transactions I, 1972. **68**(7): p. 1299-1311.
58. Airey, P.L., *Effect of irradiation on electrode processes .2. diffusion currents associated with radiolytic products.* Journal of the Chemical Society-Faraday Transactions I, 1973. **69**(12): p. 2103-2111.
59. Magee, J.L. and A. Chatterjee, *Section 4. Track reactions of radiation chemistry*, in *Kinetics of nonhomogeneous processes*, G.R.e. Freeman, Editor. 1987, John Wiley and Sons: New York.
60. Bielski, B.H.J., D.E. Cabelli, R.L. Arudi, and A.B. Ross, *Reactivity of HO_2/O_2^- radicals in aqueous-solution.* Journal of Physical and Chemical Reference Data, 1985. **14**(4): p. 1041-1100.
61. Glass, R.S., G.E. Overturf, R.A. Vankonynenburg, and R.D. McCright, *Gamma-radiation effects on corrosion .1. electrochemical mechanisms for the aqueous corrosion processes of austenitic stainless-steels relevant to nuclear waste-disposal in tuff.* Corrosion Science, 1986. **26**(8): p. 577-590.
62. Marsh, G.P., K.J. Taylor, G. Bryan, and S.E. Worthington, *The influence of radiation on the corrosion of stainless steel.* Corrosion Science, 1986. **26**(11): p. 971-982.
63. Leoni, E., C. Corbel, V. Cobut, D. Simon, D. Féron, M. Roy, and O. Raquet, *Electrochemical behaviour of gold and stainless steel under proton irradiation and active RedOx couples.* Electrochimica Acta, 2007. **53**: p. 495-510.
64. Muzeau, B., S. Perrin, C. Corbel, D. Simon, and D. Feron, *Electrochemical behaviour of stainless steel in PWR primary coolant conditions: Effects of radiolysis.* Journal of Nuclear Materials, 2011. **419**(1-3): p. 241-247.
65. Burns, W.G., R. May, and K.F. Baverstock, *Oxygen as a product of water radiolysis in high-let tracks .1. the origin of the hydroperoxyl radical in water radiolysis.* Radiation Research, 1981. **86**(1): p. 1-19.
66. Burns, W.G., W.R. Marsh, and W.S. Walters, *The gamma-irradiation-enhanced corrosion of stainless and mild steels by water in the presence of air, argon and hydrogen.* Radiation Physics and Chemistry, 1983. **21**(3): p. 259-279.
67. Elliot, A.J., D.R. McCracken, G.V. Buxton, and N.D. Wood, *Estimation of rate constants for near-diffusion-controlled reactions in water at high-temperatures.* Journal of the Chemical Society-Faraday Transactions, 1990. **86**(9): p. 1539-1547.
68. Buxton, G.V. and A.J. Elliot, *Temperature-dependence of the rate-constant for the reaction H + OH in liquid water up to 200 °C.* Journal of the Chemical Society-Faraday Transactions, 1993. **89**(3): p. 485-488.
69. Green, N.J.B., M.J. Pilling, S.M. Pimblott, and P. Clifford, *Stochastic modeling of fast kinetics in a radiation track.* Journal of Physical Chemistry, 1990. **94**(1): p. 251-258.
70. Elliot, A.J. and G.V. Buxton, *Temperature-dependence of the reactions OH + O_2^{2-} and OH + HO_2 in water up to 200 °C.* Journal of the Chemical Society-Faraday Transactions, 1992. **88**(17): p. 2465-2470.
71. Lillard, R.S., *Influence of water radiolysis products on passive film formation and reduction in a mixed radiation environment.* Corrosion Engineering Science and Technology, 2003. **38**(3): p. 192-196.
72. Bouniol, P., W. Guillot, V. Dauvois, W. Dridi, and S. Le Caer, *Original behavior of pore water radiolysis in cement-based materials containing sulfide: coupling between experiments and simulations.* Radiation Physics and Chemistry, 2018. **150**(9): p. 172-181.
73. Hanbury, R.D. and G.S. Was, *Oxide growth and dissolution on 316L stainless steel during irradiation in high temperature water.* Corrosion Science, 2019. **157**: p. 305-311.
74. Boissy, C., B. Ter-Ovanessian, N. Mary, and B. Normand, *Correlation between predictive and descriptive models to characterize the passive film - Study of pure chromium by electrochemical impedance spectroscopy.* Electrochimica Acta, 2015. **174**: p. 430-437.
75. Normand, B., A. Pierre, and J. Pagetti, *Electrochemical and surface studies of the passive layers grown on sputter-deposited nitrogen stainless-steel alloys in 1M H2SO4 solution.* Corrosion Science, 1995. **37**(10): p. 1537-1549.
76. Pourbaix, M., *Atlas of Electrochemincal Equilibria in Aqueaous Solutions, 2nd edition*. 1974, USA: National Association of Corrosion Engineers (NACE).

77. Sato, N., *An overview on the passivity of metals.* Corrosion Science, 1990. **31**: p. 1-19.
78. Matsuda, S., T. Kikuchi, and K. Sugimoto, *In situ ellipsometric determination of thickness and optical-constants of passive and transpassive films on alloy 600 in neutral solution.* Corrosion Science, 1990. **31**: p. 161-166.
79. Keddam, M., P. Ponthiaux, and V. Vivier, *Tribo-electrochemical impedance: A new technique for mechanistic study in tribocorrosion.* Electrochimica Acta, 2014. **124**: p. 3-8.
80. Dalbert, V., N. Mary, B. Normand, C. Verdu, and S. Saedlou, *In situ determinations of the wear surfaces, volumes and kinetics of repassivation: Contribution in the understanding of the tribocorrosion behaviour of a ferritic stainless steel in various pH.* Tribology International, 2020. **150**: p. 106374.
81. Okamoto, G., *Passive film of 18-8 stainless-steel structure and its function.* Corrosion Science, 1973. **13**(6): p. 471-489.
82. Ziegler, J.F., M.D. Ziegler, and J.P. Biersack, *SRIM – The stopping and range of ions in matter (2010).* Nuclear Instruments and Methods in Physics Research Section B: Beam Interactions with Materials and Atoms, 2010. **268**(11-12): p. 1818-1823.
83. Deng, P., Q.J. Peng, E.H. Han, W. Ke, C. Sun, and Z.J. Jiao, *Effect of irradiation on corrosion of 304 nuclear grade stainless steel in simulated PWR primary water.* Corrosion Science, 2017. **127**: p. 91-100.
84. Jiao, Z. and G. Was, *Oxidation of a Proton-Irradiated 316 Stainless Steel in Simulated BWR NWC Environment*, in *Proceedings of the 15th International Conference on Environmental Degradation of Materials in Nuclear Power Systems — Water Reactors*, J.T. Busby, G. Ilevbare, and P.L. Andresen, Editors. 2016, Springer International Publishing: Cham. p. 1329-1338.

Supporting Information

1. Samples

A commercial 316L austenitic stainless steel material supplied by GoodFellow, is composed of C (0.02 wt%), Si (0.49 wt%), S (0.001 wt%), P (0.035 wt%), Mn (1.79 wt%), Ni (10.1 wt%), Cr (16.7 wt%), Mo 2.03 wt%), balanced with Fe, was used in this study. The samples were 30 µm or 500 µm-thick discs of 4 cm diameter (S = 12.5 cm2).

2. Tribocorrosion device under irradiation and electrochemical measurements

2.1. Tribocorrosion device under irradiation

A diagram and a photo of this device are presented respectively in **Figure S.1 (a)** and **(b)**. This cell is placed at the outlet of an ion accelerator. The sample serves as a beam extraction window between the vacuum and the aqueous solution (here, an electrolyte consisting of an aqueous solution of Na_2SO_4, 0.02 M). The kinetic energy of the incident protons is chosen so as to stop the ions as close as possible to the stainless steel/solution interface on the solution side. The species resulting from the radiolysis of water are thus produced in the vicinity of the sample surface. If necessary, a friction movement is performed by using an alumina pin which mechanically reduces the 316L passive film. All these experiments are performed at corrosion potential in an aerated and neutral aqueous solution of sodium sulfate (0.02M) and at room temperature.
The electrochemical behavior of the 316L stainless steel is evaluated by using electrochemical techniques, which allows *in situ* measurements.

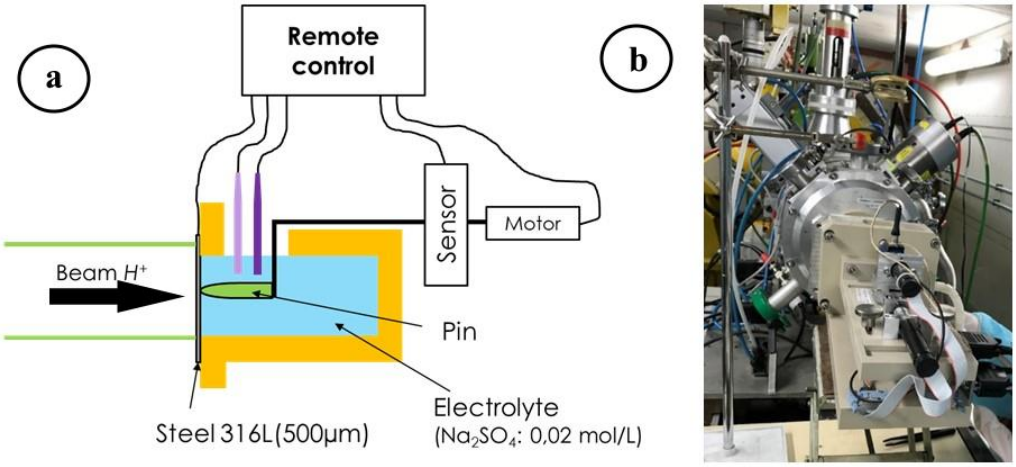

Figure S.1: a) Schematic representation of the irradiation cell and b) Photo of the cell placed at the end of the external beam line at CEMHTI cyclotron, Orléans, France [50]**.**

2.2. Electrochemical measurements

A classical three-electrode setup is connected to a potentiostat GAMRY Ref600. The working electrode is defined by the stainless-steel sheet (15 cm²), the counter electrode is Pt (50 cm²) and the reference electrode is a mercurous sulfate electrode (or MSE, E_{ref} = 0.64 V/SHE). The potential sweep rate for the polarization curve is 1 $mV.s^{-1}$ to ensure the reversibility of the measurement. The potential sweep limits are -0.5 V *vs* E_{corr} in the cathodic domain and +1.5 V *vs* E_{corr} in the anodic domain.
The measurement of the corrosion potential over time was carried out to characterize the material surface evolution. When the solution does not exhibit modifications in terms of temperature or species

concentration, the surface material tends to be passivated when the potential increases, or to be corroded when the potential decreases significantly. The polarization curves provide information on the cathodic and anodic domains, as well as on range of potential existence of the passive film. The evolution of current density gives information on electrochemical reaction kinetics [53].
The *in-situ* study of the stainless-steel passivation during irradiation is possible from the EIS measurements. To realize these measurements, the electrochemical behavior of the material must be in a stationary regime which was achieved in the absence of friction.
To ensure the reproducibility of the electrochemical measurements, the surface of the material was subjected to an electrochemical protocol in order to remove the preexisting passive film formed in the air. This protocol consists of four steps:

(i) Corrosion potential measurement for 600 s
(ii) application of the potential of -1.5 mV/MSE for 600 s to partially reduce the passive film formed in contact with air.
(iii) monitoring the evolution of the corrosion potential for 600 s in order to relax the cathodic polarization.
(iv) polarization of -330 mV/MSE applied during 3600 s.

After this conditioning, the evolution of the corrosion potential is recorded for one hour until it reaches a value of about -330 mV/MSE. This value corresponds to the corrosion potential of the material in the passive state, immersed in the neutral and aerated sulfate solution used in this study.

2.3. Irradiation conditions

Reference experiment with 16 MeV protons

In this paper, the irradiation conditions used in the previous study [49] performed at the CEMHTI cyclotron will be referred to as reference conditions. As a reminder, a 16 MeV proton beam of 10 nA intensity (i.e. a flux equal to 6.24×10^{10} H^+ s^{-1}) is used. Before being extracted from the vacuum to the cell, the protons first pass through an ionization chamber which allows monitoring the beam during the experiments. This chamber is made of three 27.17 µm thick titanium foils. The incident protons then irradiate the 500 µm thick sample and penetrate the solution. The irradiated surface is equal to 50 mm^2 (which corresponds to a flux of 1.25×10^{11} protons.cm^{-2}.s^{-1}). Under these conditions, protons lose about 0.75 MeV in the three titanium foils and then 12.3 MeV in the stainless-steel foil. The incident ions have an average kinetic energy of (2.7 ± 0.5) MeV at the stainless steel/solution interface. **Figure S. 2** shows the Lineic Energy Transfer (LET) and proton range in these irradiation conditions, obtained from a SRIM simulation [82]. The three titanium sheets are modeled by a single foil of 81.51 µm thickness.

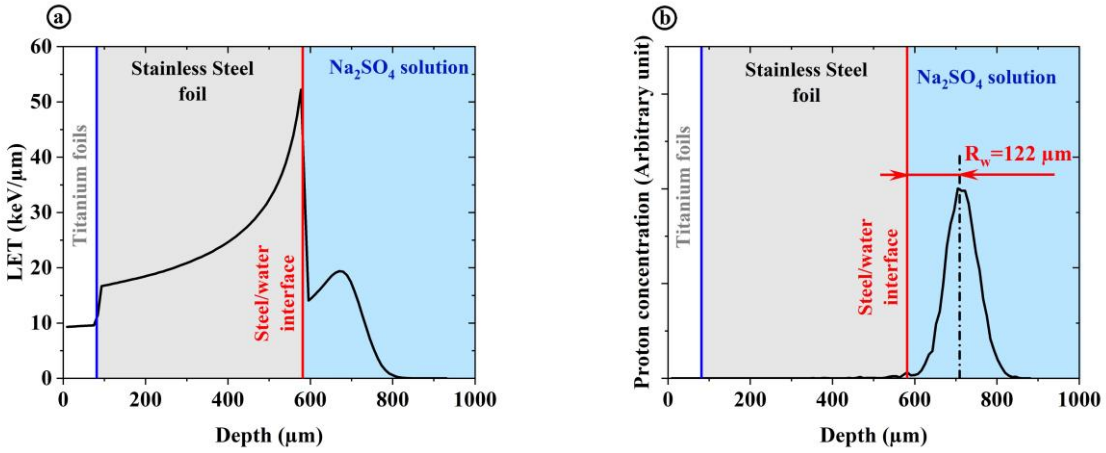

Figure S. 2: a) Proton energy deposition in the system (3 x 27.17 µm Ti + 500 µm 316L stainless steel + water), and b) Proton projected range in the same system - SRIM calculations [82]

Figure S. 2(a) shows that the LET in water is equal to 32.9 keV.μm^{-1} at 5 µm from the interface. This value decreases to 14.1 keV.μm^{-1} at 14 µm from the interface. The energy deposition beyond the interface varies, as a function of depth, in the form of a distorted Gaussian that corresponds to the Bragg peak. In **Figure S. 2(b)**, the projected range of the 16 MeV protons through titanium, stainless steel and water is

equal to (704 ± 43) µm. The protons travel an average distance in water, denoted R_w, equal to (122 ± 43) µm if the uncertainty of the sample thickness is neglected.
The proton damage in the stainless steel foil is estimated with SRIM [82] to be approximately equal to $2x10^{-9}$ dpa.s^{-1} ($7.6x10^{-6}$ dpa for 1 h) at the foil entrance and $9x10^{-9}$ dpa.s^{-1} ($3.3x10^{-5}$ dpa for 1 h) at the steel/solution interface. Under these conditions, S. S. Raiman *et al.* [46, 47] consider as negligible the role of the material damage compared to the influence of the aqueous solution radiolysis. These observations are confirmed by R. D. Hanbury *et al*. [73] who, based on [83, 84], attribute the beginning of the influence of irradiation damage on corrosion to 0.5 dpa. In conclusion, we assume that the influence of the sample damage is negligible in our experimental irradiation conditions.
In order to highlight the influence of the radiolytic species concentration, the depth of the Bragg peak maximum corresponding to the maximum of proton energy deposition in water (and thus to the maximum of radiolytic species production) had to be modified. Indeed, this modification induces the evolution of the chemical activities of the radiolysis products at the steel/solution interface. It is characterized by the measurement of the corrosion potential of the sample. The electrochemical potential is directly linked to the activities of the electroactive species by the Nernst law. Thanks to experiments performed at the IP2I 4 MV Van de Graaff accelerator, the incident proton energy can be easily modified. The next section presents the irradiation conditions.

Experiments at the IP2I 4MV VDG

Irradiation with protons of about 3 MeV requires the use of 30 µm thick samples. The beam intensity and the irradiated surface are the same as in the reference experiment, respectively 10 nA and 50 mm^2. Five kinetic energies were chosen: 2.0 MeV, 2.2 MeV, 2.7 MeV, 2.8 MeV and 3.0 MeV. **Table S 1** summarizes the different projected ranges in the system (30 µm stainless steel + aqueous sodium sulfate solution) calculated with SRIM. Let us remind that protons irradiate water which induces water radiolysis, only if projected range Rp > 30 µm. **Table S 1** specifies the energy of the protons in the vicinity of the steel/solution interface.

Table S 1: Summary of the relevant parameters related to the five proton kinetic energies used in this study: total projected range of protons Rp, LET near the interface (at 0.1, 5, and 14 µm), kinetic energy of protons at the interface, and thickness of irradiated water Rw. The last column neglects the uncertainty in the sample thicknesses. SRIM calculations [82]. n/a means not applicable.

Incident kinetic energy (MeV)	Total projected range R_p (µm)	LET in water (keV.µm^{-1}) at x µm from the interface	Proton energy at the interface, water side (MeV)	Distance R_w in water from the interface (µm)
2.0	18.6 ± 0.6	n/a	n/a	n/a
2.2	21.7 ± 0.8	n/a	n/a	n/a
2.7	30.5 ± 1.7	x = 0.1 µm : 142.6 x = 5 µm : 0.83 x = 14 µm : 0.00	0.018 ± 0.152	0.5 ± 1.7
2.8	36.4 ± 2.8	x = 0.1 µm : 149.1 x = 5 µm : 48.8 x = 14 µm : 0.16	0.385 ± 0.120	6.4 ± 2.8
3.0	52.0 ± 3.7	x = 0.1 µm : 98.2 x = 5 µm : 28.0 x = 14 µm : 39.1	1.54 ± 0.07	22.0 ± 3.7

Figure S. 3 and **Figure S. 4** show, for each proton energy, the LET profiles and the proton distributions as a function of depth. They show that the minimum energy to irradiate water, *i.e.* to irradiate exactly the interface, is about 2.7 MeV. Moreover, it can be noted from **Table S 1** and **Figure S. 3** (a) to (c) and **Figure S. 4** (a) to (b) that the energy deposited in water within 5 to 14 µm of the interface, increases as a function of the incident proton energy.
These simulations also highlight, as for the reference experiment, a strong discontinuity in the LET evolution at the interface. **Figure S. 3** (d) and (e) show that 100% of the protons are stopped in the foil. These two experiments will allow characterizing the role of the working electrode irradiation on the evolution of the corrosion potential (as already shown by B. Muzeau *et al.* [64]), which will also discriminate the role of radiolytic species in the other experiments. **Figure S. 4** (c) and (d) show that all (or almost all) protons are stopped in water. Irradiation at 2.7 MeV stops the protons at the interface as

shown in **Figure S. 3**.(f). At this energy, the stainless-steel sample is implanted, while the aqueous solution is subject to radiolysis.
Finally, **Table S 2** shows that the material damage in these irradiation conditions is very low. As explained previously, the influence of the sample damage is negligible on the electrochemical behavior of the 316L stainless steel compared to the influence of the aqueous solution radiolysis.

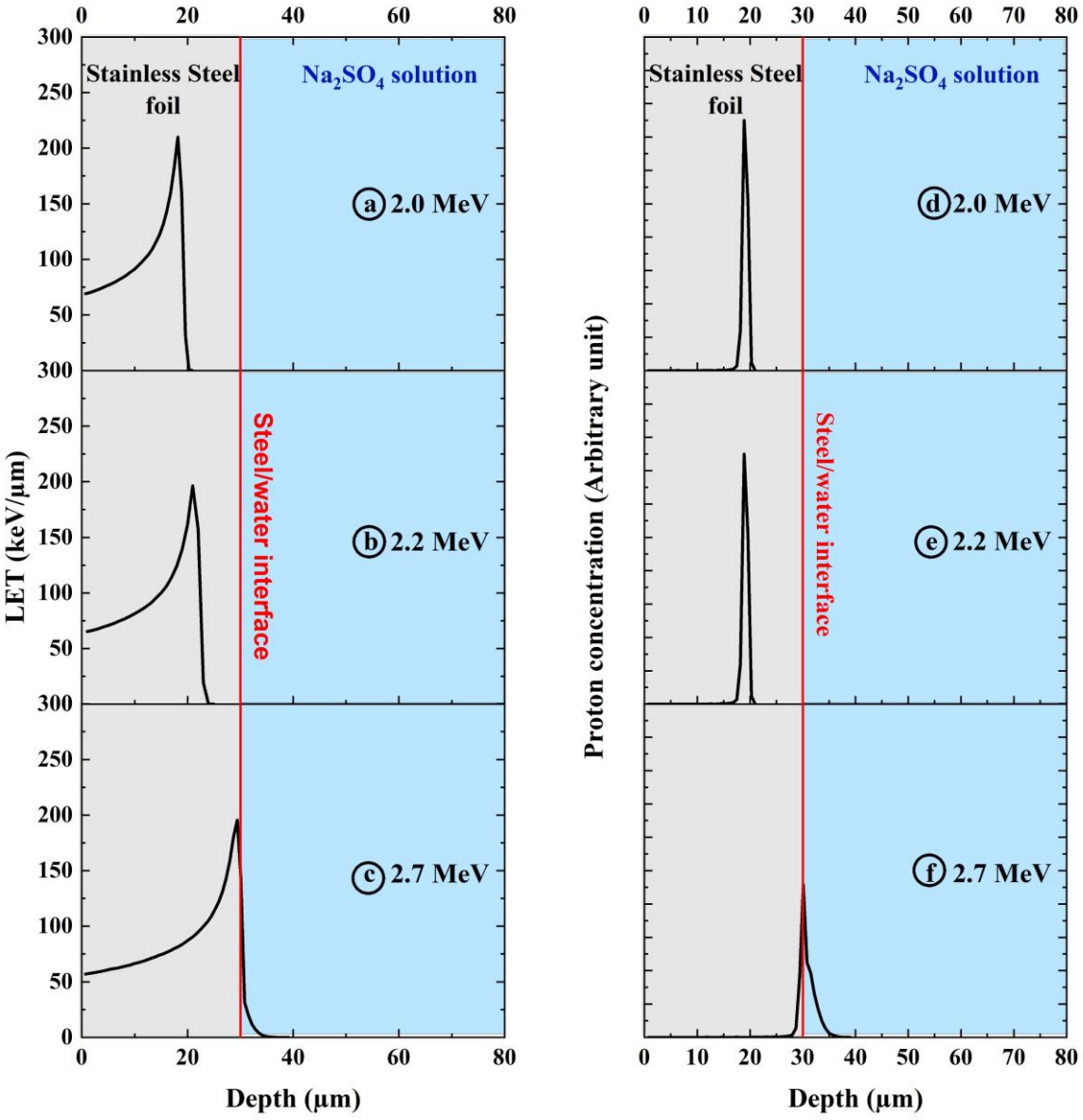

Figure S. 3: Proton energy deposition in the system (30 µm 316L stainless steel + electrolyte) for 2.0 MeV (a), 2.2 MeV (b), 2.7 MeV (c) protons and proton projected ranges for proton energies equal to 2.0 MeV (d), 2.2 MeV (e) and 2.7 MeV (f) - SRIM simulations [82]

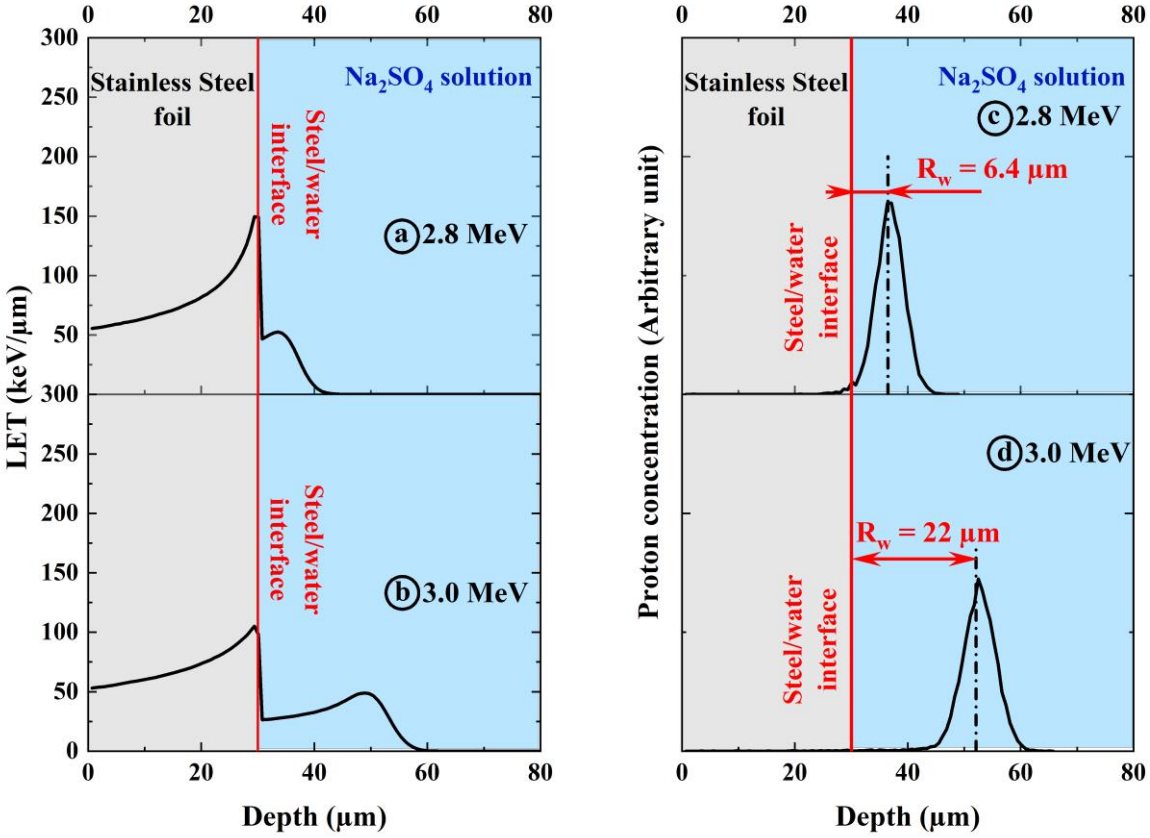

Figure S. 4: Proton energy deposition in the system (30 µm 316L stainless steel + electrolyte) for 2.8 MeV (a) and 3.0 MeV (b) protons and proton projected ranges for kinetic energies respectively equal to 2.8 MeV (c) and 3.0 MeV (d)- SRIM calculations [82]

Table S 2: Damage rates and damage for 1 h of irradiation at the entrance of the 316L stainless steel sample (e = 0) and at the interface of the 316L stainless steel (e = 30 µm). As a reminder, the interface is not irradiated at 2.0 and 2.2 MeV. Calculation performed using SRIM [82] for a beam intensity of 10 nA.

Incident kinetic energy	Damage rates at the sample entrance (e = 0)	Damage at the sample entrance (e = 0)	Maximum damage rates in the sample	Maximum damage in the sample after 1 h irradiation
MeV	dpa s^{-1}	dpa	dpa s^{-1}	dpa
2.0	9.6×10^{-9}	3.5×10^{-5}	2.3×10^{-7}	8.1×10^{-4}
2.2	9.1×10^{-9}	3.3×10^{-5}	2.2×10^{-7}	7.8×10^{-4}
			Damage rate at the sample exit (e=30 µm) dpa s^{-1}	
2.7	5.8×10^{-9}	2.1×10^{-5}	1.8×10^{-7}	6.5×10^{-4}
2.8	4.7×10^{-9}	1.7×10^{-5}	5.4×10^{-8}	2.0×10^{-4}
3.0	4.5×10^{-9}	1.6×10^{-5}	2.6×10^{-8}	9.4×10^{-5}

Doses and dose rates deposited in the aqueous solution

Doses D and average dose rates Ḋ were calculated using relationships (1 to 3):

$$\dot{D} = \frac{E.I}{e}.\frac{1}{m} \quad (1)$$

$$D = \dot{D}.t_{irr} \quad (2)$$

where: D et Ḋ are expressed in Gy and $Gy.s^{-1}$ respectively;
E: Kinetic energy of a proton at the metal/solution interface (J);
I: Proton beam intensity (A);
e: charge of a proton;
m: mass of the irradiated solution (kg). This mass was calculated by assuming that the volume V of the irradiated solution is that of a cylinder whose base area S is equal to 50 mm^2 and whose height is equal to R_w (in m).
The mass m is determined by the relation (3):

$$m = \rho.V = \rho.R_w.S \quad (3)$$

where: ρ is the density of water.

Table S 3 summarizes the data obtained and the dose values considering an irradiation time of 1 h.

Table S 3: Dose calculation and deposited dose rates in water calculated for a beam intensity I = 10 nA and for an irradiated surface S = 50 mm2. The deposited dose in water was calculated for an irradiation time of one hour.

	Incident kinetic energy (MeV)	Proton kinetic energy at the interface E (J)	Distance in water from the interface Rw (µm)	Volume of irradiated solution V (m^3)	Mass of irradiated solution m (kg)	Dose rate **Ḋ** ($Gy.s^{-1}$)	Deposited dose in water for 1 hour irradiation (Gy)
Reference experiment	16	$4.33x10^{-13}$	122	$6.1x10^{-9}$	$6.1x10^{-6}$	$4.4x10^{3}$	$1.6x10^{7}$
Experiments at the IP2I VDG	2.7	$2.88x10^{-15}$	0.5	$2.5x10^{-11}$	$2.5x10^{-8}$	$7.2x10^{3}$	$2.6x10^{7}$
	2.8	$6.17x10^{-14}$	6.4	$3.2x10^{-10}$	$3.2x10^{-7}$	$1.2x10^{4}$	$4.3x10^{7}$
	3.0	$2.47x10^{-13}$	22	$1.1x10^{-9}$	$1.1x10^{-6}$	$1.4x10^{4}$	$5.0x10^{7}$